npj | Computational Materials

www.nature.com/npjcompumats

ARTICLE OPEN

Check for updates

# Prediction of high thermoelectric performance in the low-dimensional metal halide $Cs_3Cu_2I_5$

Young-Kwang Jung[1], In Taek Han[2], Yong Churl Kim[2]✉ and Aron Walsh[1,3]✉

Metal halides have emerged as a new generation of semiconductors with applications ranging from solar cells to chemical sensors. We assess the thermoelectric potential of $Cs_3Cu_2I_5$, which has a crystal structure formed of zero-dimensional $[Cu_2I_5]^{3-}$ anionic clusters that are separated by $Cs^+$ counter cations. We find the compound exhibits the characteristics of a phonon-glass electron-crystal with a large imbalance in the conduction of heat and electrons predicted from first-principles transport theory. Strong anharmonic phonon–phonon scattering results in short-lived acoustic vibrations and an ultra-low lattice thermal conductivity (<0.1 $W\,m^{-1}\,K^{-1}$). The dispersive conduction band leads to a high electron mobility (>10 $cm^2\,V^{-1}\,s^{-1}$). For an n-type crystal at 600 K, a thermoelectric figure-of-merit *ZT* of 2.6 is found to be accessible, which for a cold source of 300 K corresponds to a thermodynamic heat-to-electricity conversion efficiency of 15%.

*npj Computational Materials* (2021)7:51 ; https://doi.org/10.1038/s41524-021-00521-9

## INTRODUCTION

The thermoelectric effect enables the direct conversion of a temperature gradient into an electric voltage and vice versa[1]. Hence, there have been many studies to discover new materials that show high-energy conversion efficiency[2–4]. The performance of thermoelectric materials can conveniently be evaluated by the dimensionless figure of merit *ZT*, which is defined as

$$ZT = \frac{S^2\sigma T}{\kappa_{elec} + \kappa_{latt}} \quad (1)$$

where *S* is the Seebeck coefficient, $\sigma$ is the electrical conductivity, *T* is the temperature, $\kappa_{elec}$ is the electronic thermal conductivity, and $\kappa_{latt}$ is the lattice thermal conductivity. Achieving high Seebeck coefficient and electrical conductivity with low electronic and lattice thermal conductivity is therefore the formula for success. In practice, there are limits in the accessible property space for semiconductors, including the positive correlation between Seebeck coefficient, electrical conductivity, and electronic thermal conductivity[5]. Thus, low lattice thermal conductivity is one of promising design strategies for higher performing thermoelectric materials.

We have been inspired by observations of the thermoelectric effect in halide perovskites[6–8], where a record *ZT* of 0.14 was recently achieved[9]. However, there is a strong desire to move away from heavy and toxic elements such as Pb. $Cs_3Cu_2I_5$ is an alternative metal halide that has drawn attention for optoelectronics. Since the report of its application in blue light emitting diodes (LEDs)[10], the optical properties of this material has been intensively investigated[11–13]. $Cs_3Cu_2I_5$ has an unusual crystal structure where $[Cu_2I_5]^{3-}$ clusters are surrounded and isolated by $Cs^+$ cations. Unlike perovskites, for example, this *Pnma* structure has no through-bond connectivity between neighboring anionic fragments. The atomic structure of $Cs_3Cu_2I_5$ was recently linked to its optical properties including self-trapped excitons and a large Stokes shift in the photoluminescence[11,13]. Complex crystal structures have been associated with low thermal conductivity in the past[14]. Indeed, a value of 0.15 $W\,m^{-1}\,K^{-1}$ was recently measured in $[Mn(C_2H_6OS)_6]I_4$, which shares a low-dimensional crystal structure[15].

In this study, we assess the thermoelectric potential of $Cs_3Cu_2I_5$. We calculate the thermal transport using anharmonic lattice dynamics, which highlights an ultra-low conductivity for the perfect crystal that is below the limit of standard models. We further investigate electron transport through an ab initio description of carrier scattering. The same low-dimensional crystal structure that gives rise to ultra-low thermal transport supports efficient electron transport with a room temperature electron mobility of 18.2 $cm^2\,V^{-1}\,s^{-1}$. We predict that $Cs_3Cu_2I_5$ exhibits the characteristics of an ideal thermoelectric semiconductor—a phonon-glass electron-crystal—with an accessible *ZT* of greater than 2.

## RESULTS

### Basic bulk properties

The ground-state *Pnma* crystal structure of $Cs_3Cu_2I_5$ is illustrated in Fig. 1a. Cs atoms reside at **4c** and **8d** Wyckoff positions, Cu atoms reside at **4c**, and I atoms reside at three distinct **4c** and **8d**. An associated electron localization function (ELF) plot could be found in Supplementary Fig. 1. The atomic structure is similar to low-dimensional perovskite-inspired materials such as $Cs_4PbBr_6$ where metal halide anion clusters are surrounded and isolated by cation counter parts (effective 0D connectivity)[16,17]. However, due to distinct size and orbital configuration of Cu(I) $3d^{10}4s^0$, it does not form octahedral clusters like Pb(II) $5d^{10}6s^2$ [18]. The calculated equilibrium lattice constants of $a_0 = 10.06$ Å $b_0 = 11.53$ Å and $c_0 = 14.15$ Å match well with values determined from X-ray diffraction ($a_0^{exp} = 10.19$ Å $b_0^{exp} = 11.66$ Å and $c_0^{exp} = 14.40$Å)[10]. By fitting the energy-volume relationship to the third-order Birch-Murnaghan equation-of-state[19], we obtained a bulk modulus of $B_0 = 10.6$ GPa for $Cs_3Cu_2I_5$, which is even softer than $Cs_4PbBr_6$ ($B_0 = 12.1$ GPa)[20]. For comparison, the bulk modulus of Si is ~100 GPa.

[1]Department of Materials Science and Engineering, Yonsei University, Seoul, South Korea. [2]Samsung Advanced Institute of Technology (SAIT), Samsung Electronics Materials Research Complex, Youngtong, Suwon, South Korea. [3]Department of Materials, Imperial College London, London, UK. ✉email: yongchurl.kim@samsung.com; a.walsh@imperial.ac.uk

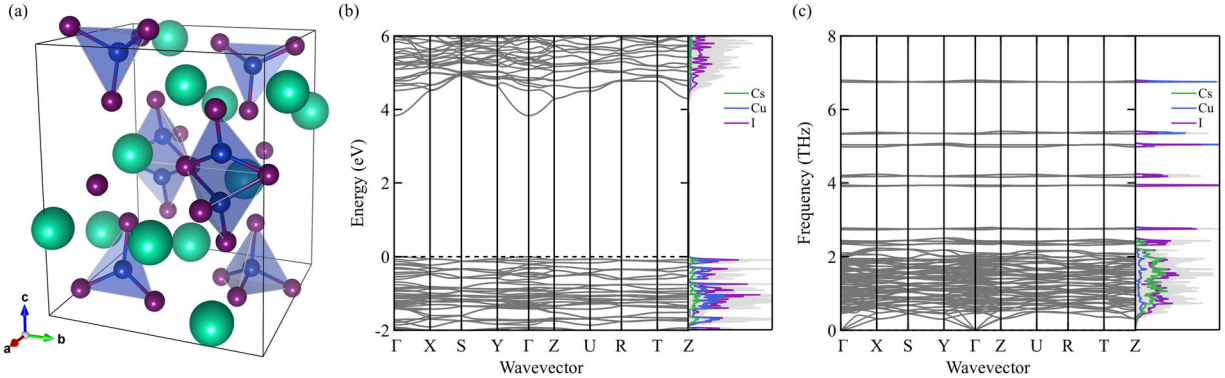


**Fig. 1 Crystal and band structures. a** Crystal structure, **b** electronic band structure (the valence band maximum is set to 0 eV), and **c** phonon band structure of $Cs_3Cu_2I_5$. Atom projected density of states are plotted on the right side of electronic and phonon band structures, where Cs, Cu, and I contributions are shown in green, blue, and purple lines, respectively.

The electronic band structure is shown in Fig. 1b. This has been calculated using density functional theory (DFT) with the hybrid HSE06 functional using Wannier interpolation[21–23]. The upper valence band, formed of Cu 3*d* and I 5*p* orbitals, is found to be flat in reciprocal space (i.e., short-range interactions in real space). At the same time, the lower conduction band is dispersive and formed of Cu 4*s* and I 5*s* (see Supplementary Fig. 2). The associated electron effective mass is 0.3 $m_e$, which is comparable to other wide band gap semiconductors such as $In_2O_3$ and ZnO. The behavior contrasts with other 0D metal halides that have a flat conduction band dispersion (e.g., $Cs_4PbBr_6$) where the lower conduction band is formed from Pb 6*p*)[20]. The dispersive nature and isotropic overlap of the Cu 4*s* orbitals contributes to the low electron effective mass in $Cs_3Cu_2I_5$. For $Cs_3Cu_2I_5$, the direct band gap of 3.82 eV at Γ point is obtained from HSE06 calculation, which matches well with measured values for the optical absorption onset[12].

The phonon dispersion of $Cs_3Cu_2I_5$ is shown in Fig. 1c. The lattice vibrations were calculated using the finite-displacement method and the PBEsol functional due to its good description of the crystal structure and phonon properties of semiconductors[24–26]. Since the primitive cell contains 40 atoms, there are 120 phonon bands where 3 acoustic branches are followed by a series of localized optic modes up to 7 THz. We find no imaginary frequencies, which confirms dynamic stability for this phase of $Cs_3Cu_2I_5$. There is a dense block of optic modes that run from 0.5–2.5 THz involving the collection motion of group atoms, such as relative tilting of $[Cu_2I_5]^{3-}$ clusters. As a result, acoustic branches are strongly suppressed < 0.5 THz. The presence of this dense block of low-energy phonons just above the acoustic branch creates many energy and momentum allowed scattering pathways that significantly reduce the lifetime of the heat carrying acoustic modes. Such a high density of low-frequency modes also explains the small bulk modulus. Inspection of the eigenvectors at Γ point shows that acoustic modes are simple translation of the entire lattice sites, while the highest frequency optic mode involves Cu–Cu stretching within each cluster. Zoomed electronic and phonon band structures are shown in Supplementary Fig. 3.

## Ultra-low lattice thermal conductivity

Next we consider the lattice thermal conductivity ($\kappa_{latt}$) by taking into account three-phonon scattering. This approach should provide an upper limit to the thermal transport as additional scattering events can be active in real crystals. Three-phonon scattering is subject to energy and momentum conservation rules for phonon creation and annihilation; however, the flat nature of the phonon dispersion for $Cs_3Cu_2I_5$ opens up many allowed channels. Owing to structural anisotropy, the conductivity along three principal directions ($\kappa_{xx}$, $\kappa_{yy}$, and $\kappa_{zz}$) differs, as shown in Fig. 2a. The largest values are found along the *b* axis, which is parallel to the base of the trigonal-planar Cu atoms, and has larger group velocities. The isotropically-averaged conductivity ($\kappa_{iso}$) is 0.018 W m$^{-1}$ K$^{-1}$ at room temperature. We tested both the single mode relaxation time approximation (RTA) and direct solution of linearized phonon Boltzmann equation (LBTE)[27], which are in good agreement. The LBTE value is ~10% lower across the relevant temperature range (see Supplementary Fig. 4).

The lattice thermal conductivity is among the lowest reported for bulk crystals. For instance, $\kappa_{iso}$ of $CH_3NH_3PbI_3$[28], $Sn_2S_3$[29], and $Cs_2BiAgBr_6$[30] was reported to be 0.05, 0.06, and 0.07 W m$^{-1}$ K$^{-1}$, respectively, at similar levels of theory. This values is also lower than the minimum lattice thermal conductivity ($\kappa_{min}$) expected from diffuson-mediated thermal transport[31], which can be estimated from:

$$\kappa_{min} = 0.76 k_B \frac{v_s}{V_a^{2/3}} \quad (2)$$

where $k_B$ is Boltzmann constant, $v_s$ is the speed of sound, and $V_a$ is the volume of unit cell per atom. The model predicts $\kappa_{min}$ of 0.1 W m$^{-1}$ K$^{-1}$ for $Cs_3Cu_2I_5$. To understand the origin of such a low-lattice thermal conductivity, below the prediction of the analytical model, we analyzed the modal contributions to the net transport. Extremely short acoustic phonon lifetimes of sub 12 ps (Fig. 2b) result in short phonon mean-free paths of below 24 nm. Thus, we conclude that high-acoustic phonon-scattering rates are the main origin of the ultra-low lattice thermal conductivity in $Cs_3Cu_2I_5$ despite their moderate group velocity and heat capacity. A full breakdown of the modal contributions is provided in Supplementary Fig. 5. The dense block of low-energy phonons have similarity to the states created by the $CH_3NH_3$ cation in $CH_3NH_3PbI_3$[32]. Although a similar computational approach has been shown to give good agreement with experimental measurements on the thermoelectric propoerties of metal halides such as $CsSnI_3$[33], it should be noted that perturbation theory based on three-phonon scattering is pushed to its limits of applicability in such cases[34,35]. We propose that $Cs_3Cu_2I_5$ is ideal for testing more sophisticated treatments of anharmonicity including self-consistent phonon theory[36,37].

## Electronic transport properties

Given the wide electronic band gap of 3.82 eV, pristine $Cs_3Cu_2I_5$ is an insulator as there is no significant thermal population of electrons and holes. However, high carrier concentrations (~$10^{21}$ cm$^{-3}$) can be achieved in such wide band gap semiconductors by doping (e.g. Al or Ga doped ZnO[38,39] and Zr or W doped $In_2O_3$[40,41]), which is an active research topic in transparent conductors[42]. Motivated by the small electron effective mass, we performed electron transport simulations under *n*-type doping conditions, in the range $10^{16}$–$10^{20}$ cm$^{-3}$. Our preliminary

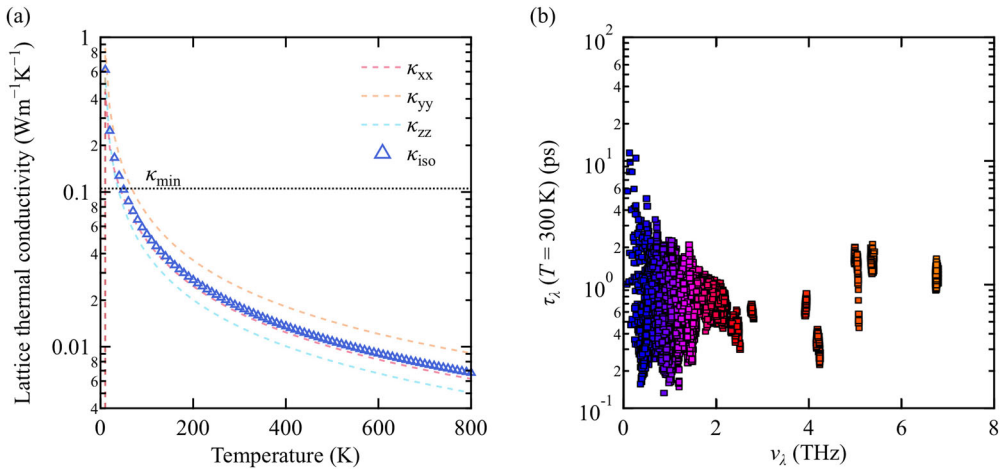


**Fig. 2 Lattice thermal conductivity analysis. a** Lattice thermal conductivity, calculated from direct solution of linearized phonon Boltzmann equation, of $Cs_3Cu_2I_5$ as a function of temperature. The red ($\kappa_{xx}$), orange ($\kappa_{yy}$), and sky blue ($\kappa_{zz}$) dotted lines indicate direction dependent lattice thermal conductivity that are parallel to *a*-, *b*-, and *c*-axes of the primitive cell. The blue triangle markers ($\kappa_{iso}$) show the isotropic average of the thermal conductivity tensor ($\kappa_{iso} = [\kappa_{xx} + \kappa_{yy} + \kappa_{zz}]/3$). $\kappa_{min}$ refers to the minimum lattice thermal conductivity in a diffuson-mediated transport model. **b** Phonon lifetime ($\tau_\lambda$) at 300 K as a function of mode frequency ($\nu_\lambda$). The color gradient is given by phonon band index.

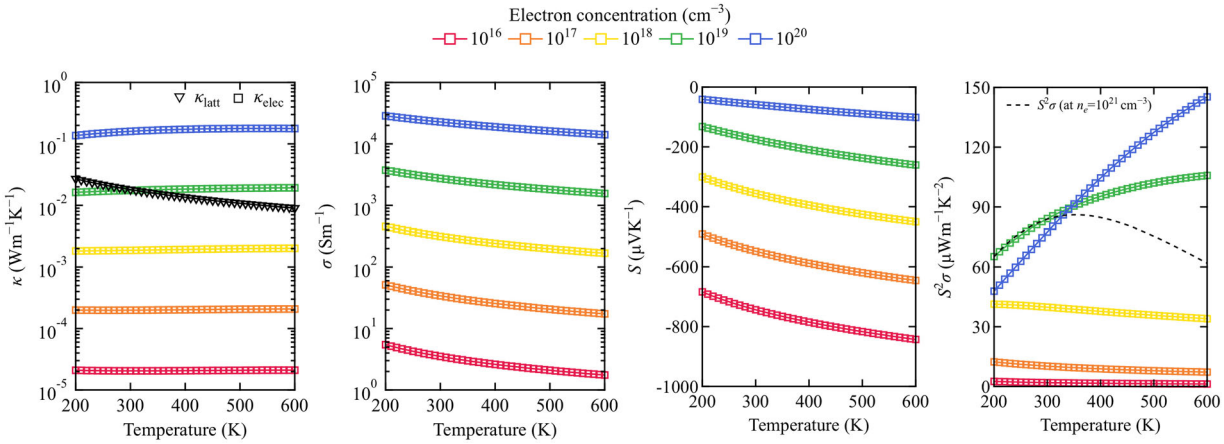


**Fig. 3 Transport property analysis.** Electronic transport properties of $Cs_3Cu_2I_5$ as a function of temperature and carrier concentration. $\kappa$ stands for the thermal conductivity, where $\kappa_{latt}$ is contribution of phonons and $\kappa_{elec}$ is contribution of electrons. $\sigma$ stands for the electrical conductivity, $S$ stands for the Seebeck coefficient, and $S^2\sigma$ denotes the power factor.

calculations suggest that $Ba_{Cs}^{+}$ has a shallow donor level, which could support an *n*-type doping density. The associated electrical transport properties are shown in Fig. 3. The electronic thermal conductivity remains lower than the lattice thermal conductivity for $n_e \leq 10^{18}$ cm$^{-3}$, which means that thermal losses through phonons will be more critical for thermoelectric applications. Once the carrier concentration exceeds $10^{19}$ cm$^{-3}$, the electronic component becomes dominant.

The electron mobility of $Cs_3Cu_2I_5$ is found to be limited by optical phonon scattering, followed by ionized impurity and acoustic deformation potential scattering (see Supplementary Fig. 6a), which is consistent with the behavior of other polar semiconductors[43,44]. The electron relaxation times and associated materials properties are given in Table 1. The electron mobility at room temperature is 18.2 cm$^2$ V$^{-1}$ s$^{-1}$ for an *n*-type doping concentration of $4 \times 10^{18}$ cm$^{-3}$. The simpler constant-relaxation time approximation (CRT), assuming the standard $\tau = 10^{-14}$ s, predicts an overestimated value of 60.1 cm$^2$ V$^{-1}$ s$^{-1}$ (see Supplementary Fig. 6b). The electrical conductivity increases from around 3.5 to $2.3 \times 10^4$ Sm$^{-1}$, while the absolute value of

**Table 1.** Three types of electron scattering mechanism are considered as implemented in AMSET[44]: (i) acoustic deformation potential (ADP); (ii) ionized impurity (IMP); (iii) polar-optical phonon (POP). $\tau_T$ are the lifetimes for a given scattering process at $T$ in unit of fs where electron concentration is assumed to be $4 \times 10^{18}$ cm$^{-3}$, $a_v^{VBM}$ & $a_v^{CBM}$ are the volume deformation potential of valence band maximum (VBM) and conduction band minimum (CBM) in unit of eV, $B_0$ is the bulk modulus in unit of GPa, $Z$ is the charge of electron donor dopant, $\epsilon_0$ is the static dielectric constant, $\epsilon_\infty$ is the electronic contribution to the static dielectric constant, and $\omega_{po}$ is the polar-optical phonon frequency in THz.

| | | | | | |
|---|---|---|---|---|---|
| ADP | $\tau_{300\,K}$ | $\tau_{600\,K}$ | $a_v^{VBM}$ | $a_v^{CBM}$ | $B_0$ |
| | 54.4 | 27.1 | − 1.08 | − 3.30 | 10.55 |
| IMP | $\tau_{300\,K}$ | $\tau_{600\,K}$ | $Z$ | $\epsilon_0$ | |
| | 5.65 | 4.17 | 1 | 7.54 | |
| POP | $\tau_{300\,K}$ | $\tau_{600\,K}$ | $\omega_{po}$ | $\epsilon_\infty$ | $\epsilon_0$ |
| | 1.31 | 0.66 | 1.78 | 3.79 | 7.54 |

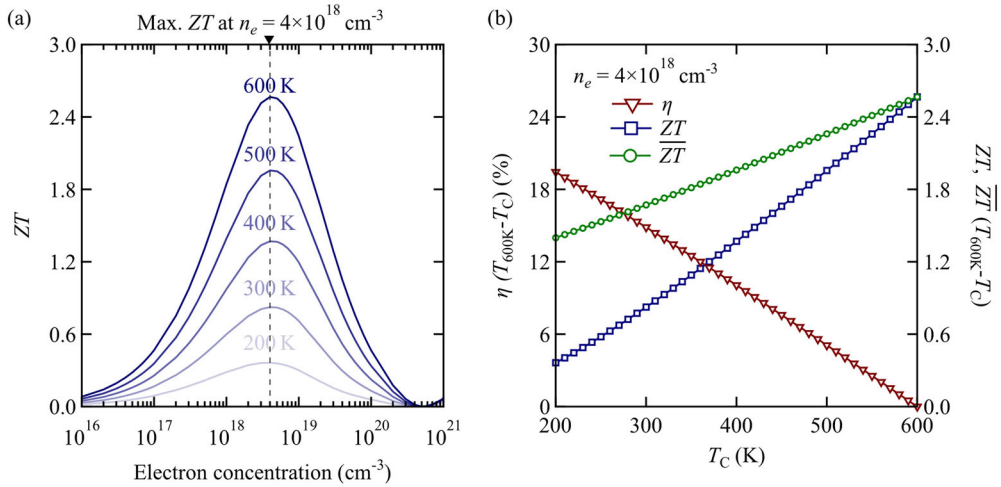


**Fig. 4 *ZT* and efficiency prediction. a** Predicted *ZT* values of $Cs_3Cu_2I_5$ as a function of temperature and carrier concentration. **b** Estimated thermodynamic efficiency ($\eta$, brown triangles) and average *ZT* ($\overline{ZT}$, dark green circles) at electron concentration ($n_e$) of $4\times10^{18}$ cm$^{-3}$ over temperature range of $T_C$–$T_H$. $T_H$ is fixed as 600 K. *ZT* at the given temperature is indicated by navy squares.

Seebeck coefficient decreases from around 750 to 60 μV K$^{-1}$ in the given doping range at room temperature. The power factor ($S^2\sigma$) is maximized around $10^{20}$ cm$^{-3}$ at a value of 150 μW m$^{-1}$ K$^{-2}$.

### Thermoelectric performance prediction

By combining the results on thermal and electron transport, the predicted *ZT* of $Cs_3Cu_2I_5$ as a function *n*-type doping concentration and temperature is shown in Fig. 4a. Here, the temperature range is set to 600 K as prediction for temperature region near the melting temperature of 663 K[11] will not be reliable due to possibility of evaporation and mass loss, which is beyond limit of our simulation techniques. At 600 K maximum *ZT* is predicted to be 2.57 where a *n*-type doping concentration of $4\times10^{18}$ cm$^{-3}$ is assumed. Above this doping level, electronic thermal conductivity causes *ZT* to decrease. When the anisotropic nature of transport properties along the principal axes is considered, *ZT* can be maximized along *c* with a *ZT* of 3.35 due to a combination of lower lattice thermal conductivity and higher power factor. A full analysis of the anisotropy is found in Supplementary Fig. 7. The maximum *ZT* of $Cs_3Cu_2I_5$ predicted is the highest for any metal halide compound. While the power factor is moderate, *ZT* is enhanced by the ultra-low lattice thermal conductivity. Although there have been attempts to make thermoelectric devices using metal halide perovksites[8], the performance has been limited thus far. A value of $ZT = 0.14$ was achieved for $CsSnI_3$[7], with a similar $ZT = 0.13$ for $CH_3NH_3SnI_3$[6]. On the other hand Pb-based halide perovskites have shown negligible thermoelectric response[6,8]. The predicted *ZT* of $Cs_3Cu_2I_5$ is comparable to other emerging thermoelectric compounds. For instance, the maximum *ZT* of $CsBi_4Te_6$, $Zn_4Sb_3$, and, SnSe are 0.8 at 225 K[45], 1.4 at 750 K[46], 2.6 at 923 K[47], respectively.

The efficiency of a thermoelectric device ($\eta$) is not determined by maximum *ZT* at a single temperature but depends on the average *ZT* ($\overline{ZT}$) over a wide temperature range following

$$\eta = \frac{T_H - T_C}{T_H}\frac{\sqrt{1+\overline{ZT}}-1}{\sqrt{1+\overline{ZT}}+\frac{T_C}{T_H}} \quad (3)$$

where $T_H$ and $T_C$ are the temperature of hot side and cold side of the device, and $\overline{ZT} = \frac{1}{(T_H - T_C)}\int_{T_C}^{T_H} ZT dT$. To further evaluate the performance of *n*-type $Cs_3Cu_2I_5$-based thermoelectric devices, we plot efficiency over temperature gradient where $T_H$ is fixed as 600 K in Fig. 4b. The average $\overline{ZT}$ of 1.67 leads to a predicted efficiency of 14.9% over a 300–600 K temperature gradient, where $n_e$ is $4\times10^{18}$ cm$^{-3}$.

Beyond the performance of the bulk metal halide, existing crystal engineering approaches could also be applied to $Cs_3Cu_2I_5$. Cation (e.g., $Cs_{1-x}Rb_x$) and/or anion (e.g., $I_{1-x}Br_x$) substitution is one way to tune *ZT*, which has been widely adopted to modulate optoelectronic properties in metal halide perovskites[11,48–50]. Such ion substitution could further reduce the lattice thermal conductivity due to the additional alloy-scattering channels[51,52]. In practice, recent reports have shown improved values of *ZT* by partially replacing I in $CsSnI_3$, and achieved *ZT* of 0.14 for $CsSnCl_{3-x}I_x$[9] and 0.15 for $CsSnBr_{3-x}I_x$[53].

## DISCUSSION

We have demonstrated the potential of a metal halide based on a low-dimensional bonding network for heat-to-electricity conversion. $Cs_3Cu_2I_5$ is predicted to support efficient electron transport with slow heat transport. An ultra-low lattice thermal conductivity of < 0.1 W m$^{-1}$ K$^{-1}$ is predicted, among the lowest reported for a crystalline solid. Owing to its effective thermal insulation, the maximum *ZT* of *n*-type $Cs_3Cu_2I_5$ is predicted to be 2.57 at 600 K, which is over 10 times larger than the current record of 0.15 in $CsSnBr_{3-x}I_x$ and close to the champion value of 2.6 achieved in SnSe. By alloying or nanostructuring, the *ZT* may be even further enhanced. Our work therefore provides an alternative avenue for developing high-performing thermoelectric materials. Those materials with low-dimensional crystal structure and dispersive band structure (e.g., band edges with *s-s* orbital overlap) could be attractive candidates. The main bottleneck to realizing such a high *ZT* will be achieving appropriate carrier concentrations. Further investigations are required to enhance the electrical conductivity of multinary metal halides beyond their natural limits.

## METHODS

### Thermal transport

The thermal physics was simulated from lattice dynamics calculations considering the phonon eigenvectors, eigenvalues, and lifetimes due to three-phonon scattering. First, harmonic phonon analysis was performed using the Phonopy[54] code with a finite-displacement step of 0.01 Å. A 2 × 2 × 2 supercell expansion of the relaxed unit cell, containing 320 atoms, was employed. In total 36 symmetry-reduced displacements were considered. Then, anharmonic calculations were performed using the Phono3py[55] code with a finite-displacement step of 0.03 Å. For the third-order force constants, 7818 symmetry-reduced displacements were considered in the 40 atom unit cell. Γ-centered **q**-meshes of 24 × 24 × 18 and 8 × 8 × 6 were used to compute the phonon density of states and

lattice thermal conductivity. Symmetrization of the force constants was applied where the maximum drift value of the third order force constants is 0.73 eV Å$^{-1}$ before symmetrization. All norms of the atomic forces sets and a convergence test on our thermal transport calculations over **q**-meshes can be found in Supplementary Fig. 8.

The lifetimes are solved through a direct solution of the linearized Boltzmann transport equation (LBTE)[27]. Then the macroscopic lattice thermal conductivity $\kappa_{\text{latt}}$ is obtained by summing over phonon band indices ($\nu_\lambda$) and wavevectors (**q**), while normalizing by the volume of the unit cell:

$$\kappa_{\text{latt}} = \frac{1}{NV_0}\sum_\lambda \kappa_\lambda = \frac{1}{NV_0}\sum_\lambda C_\lambda \mathbf{v}_\lambda \otimes \mathbf{v}_\lambda \tau_\lambda \tag{4}$$

where $N$ is the number of unit cells in the crystal (equivalent to the number of wavevectors included in the Brillouin zone summation) and $V_0$ is the volume of the crystallographic unit cell. $\kappa_\lambda$ contains the product of the modal heat capacity ($C_\lambda$), group velocity ($\mathbf{v}_\lambda$), and phonon mean-free path ($\mathbf{v}_\lambda \times \tau_\lambda$, where $\tau_\lambda$ is the phonon lifetime). Graphical analyses of the modal contributions to lattice thermal conductivity and the atomic force sets used for the thermal conductivity calculations were performed using the Phono3py-Power-Tool code[56].

## Electron transport

The transport of electrons was simulated by considering three scattering processes, with a characteristic scattering time following Matthiessen's rule:

$$\frac{1}{\tau_e} = \frac{1}{\tau^{\text{ADP}}} + \frac{1}{\tau^{\text{IMP}}} + \frac{1}{\tau^{\text{POP}}} \tag{5}$$

Each component of $\tau_e$ was calculated from Fermi's golden rule:

$$\tilde{\tau}^{-1}_{n\mathbf{k}\to m\mathbf{k}+\mathbf{q}} = \frac{2\pi}{\hbar}|g_{nm}(\mathbf{k},\mathbf{q})|^2 \delta(\varepsilon_{n\mathbf{k}} - \varepsilon_{m\mathbf{k}+\mathbf{q}}) \tag{6}$$

where $\hbar$ is the reduced Planck constant, $\varepsilon$ is the electron energy, $\delta$ is the Dirac delta function and $g$ is the coupling matrix element. Matrix elements due to the acoustic deformation potential (ADP), ionized impurity (IMP), and polar-optical phonon (POP) mechanisms are considered:

$$g^{\text{ADP}}_{nm}(\mathbf{k},\mathbf{q}) = \left[\frac{k_B T a_v^2}{B_0}\right]^{\frac{1}{2}} \langle \psi_{m\mathbf{k}+\mathbf{q}} | \psi_{n\mathbf{k}} \rangle \tag{7}$$

$$g^{\text{IMP}}_{nm}(\mathbf{k},\mathbf{q}) = \left[\frac{n_{\text{ii}} Z^2 e^2}{\epsilon_0}\right]^{\frac{1}{2}} \frac{\langle \psi_{m\mathbf{k}+\mathbf{q}} | \psi_{n\mathbf{k}} \rangle}{|\mathbf{q}|^2 + \beta^2}, \tag{8}$$

$$g^{\text{POP}}_{nm}(\mathbf{k},\mathbf{q}) = \left[\frac{\hbar\omega_{\text{po}}}{2}\left(\frac{1}{\epsilon_\infty} - \frac{1}{\epsilon_0}\right)\right]^{\frac{1}{2}} \frac{\langle \psi_{m\mathbf{k}+\mathbf{q}} | \psi_{n\mathbf{k}} \rangle}{|\mathbf{q}|} \tag{9}$$

The formalism is implemented in the ab initio scattering and transport (AMSET) package[44]. The required material parameters, including dielectric constants $\epsilon$, phonon frequency $\omega$, bulk modulus $B_0$, deformation potential $a$, were all calculated from first-principles. The associated Seebeck coefficient, electrical conductivity, and electronic component of the thermal conductivity are calculated from the Onsager transport coefficients[57]. An interpolation factor of 10 was used during AMSET routine.

## Density functional theory

All of the underlying total energy and electronic structure calculations were performed based on Kohn–Sham density functional theory[58], where periodic boundary conditions are considered to represent the extended crystal. The Vienna Ab Initio Simulation Package (VASP)[59,60] was used with Projector augmented-wave (PAW)[61,62] method where the valence states of Cs, Cu, and I are treated explicitly by 9($5s^2 5p^6 6s^1$), 17($2p^6 3d^{10} 4s^1$), and 7 ($5s^2 5p^5$) electrons, respectively.

The Perdew–Burke–Ernzerhof exchange-correlation functional revised for solids (PBEsol)[63] with the plane-wave kinetic energy cutoff of 700 eV was used to optimize crystal structure including the internal positions. A $3\times3\times2$ Γ-centered **k**-mesh was adopted for structure optimization, where the convergence criteria were set to $10^{-6}$ eV and $10^{-3}$ eV Å$^{-1}$ for total energy and atomic forces, respectively. This crystal structure was then used consistently for all transport calculations.

For thermal transport, the same DFT setup was employed and the Brillouin zone was sampled with $2\times2\times1$ **k**-mesh for the $2\times2\times2$ supercell. For electron transport, the required Kohn–Sham wavefunctions ($\psi$) were generated using the hybrid functional HSE06[64,65]. Here we used a dense $6\times6\times4$ Γ-centered **k**-mesh for better sampling of the electronic Brillouin zone, but lowered the kinetic energy cutoff to 400 eV in order to reduce the computational load. A convergence test on our electronic transport calculations over **k**-meshes and interpolation factors can be found in Supplementary Fig. 9.

## DATA AVAILABILITY

An online repository containing the optimized crystal structure, force constant sets, and raw AMSET input/output files have been made available at https://doi.org/10.5281/zenodo.4576211.

## CODE AVAILABILITY

Post-processing scripts for AMSET package have been made available at https://doi.org/10.5281/zenodo.4576211.

Received: 27 November 2020; Accepted: 11 March 2021;
Published online: 14 April 2021

## REFERENCES

1. Goldsmid, H. J. *Introduction to Thermoelectricity*. (Springer-Verlag, Berlin Heidelberg, 2010).
2. Tan, G., Zhao, L.-D. & Kanatzidis, M. G. Rationally designing high-performance bulk thermoelectric materials. *Chem. Rev.* **116**, 12123–12149 (2016).
3. Gorai, P., Stevanović, V. & Toberer, E. S. C. *Nat. Rev. Mater.* **2**, 1–16 (2017).
4. Jain, A., Shin, Y. & Persson, K. A. Computational predictions of energy materials using density functional theory. *Nat. Rev. Mater.* **1**, 1–13 (2016).
5. Snyder, G. J. in *Energy Harvesting Technologies*, 325–336 (Springer, 2009).
6. Mettan, X. et al. Tuning of the thermoelectric figure of merit of $CH_3NH_3MI_3$ (M = Pb,Sn) photovoltaic perovskites. *J. Phys. Chem. C.* **119**, 11506–11510 (2015).
7. Saini, S., Baranwal, A. K., Yabuki, T., Hayase, S. & Miyazaki, K. Growth of halide perovskites thin films for thermoelectric applications. *MRS Adv.* **4**, 1719–1725 (2019).
8. Haque, M. A., Kee, S., Villalva, D. R., Ong, W. L. & Baran, D. Halide perovskites: thermal transport and prospects for thermoelectricity. *Adv. Sci.* **7**, 1903389 (2020).
9. Liu, T. et al. Enhanced control of self-doping in halide perovskites for improved thermoelectric performance. *Nat. Commun.* **10**, 5750 (2019).
10. Jun, T. et al. Lead-free highly efficient blue-emitting $Cs_3Cu_2I_5$ with 0D electronic structure. *Adv. Mater.* **30**, 1804547 (2018).
11. Roccanova, R. et al. Near-unity photoluminescence quantum yield in blue-emitting $Cs_3Cu_2Br_{5-x}I_x$ ($0 \le x \le 5$). *ACS Appl. Electron. Mater.* **1**, 269–274 (2019).
12. Chen, H. et al. Multiple self-trapped emissions in the lead-free halide $Cs_3Cu_2I_5$. *J. Phys. Chem. Lett.* **11**, 4326–4330 (2020).
13. Lian, L. et al. Photophysics in $Cs_3Cu_2X_5$ (X = Cl, Br, or I): highly luminescent self-trapped excitons from local structure symmetrization. *Chem. Mater.* **32**, 3462–3468 (2020).
14. Snyder, G. J. & Toberer, E. S. Complex thermoelectric materials. *Nat. Mater.* **7**, 105–114 (2008).
15. Haque, M. A. et al. A 0D lead-free hybrid crystal with ultralow thermal conductivity. *Adv. Funct. Mater.* **29**, 1809166 (2019).
16. Akkerman, Q. A. & Manna, L. What defines a halide perovskite? *ACS Energy Lett.* **5**, 604–610 (2020).
17. Huang, Y.-T., Kavanagh, S. R., Scanlon, D. O., Walsh, A. & Hoye, R. L. Z. Perovskite-inspired materials for photovoltaics–from design to devices. *Nanotechnology* **32**, 132004 (2021).
18. Gillespie, R. & Nyholm, R. Inorganic stereochemistry. *Quart. Rev. Chem. Soc.* **11**, 339–380 (1957).
19. Birch, F. Finite elastic strain of cubic crystals. *Phys. Rev.* **71**, 809–824 (1947).
20. Jung, Y.-K. et al. Intrinsic doping limit and defect-assisted luminescence in $Cs_4PbBr_6$. *J. Mater. Chem. A* **7**, 20254–20261 (2019).
21. Marzari, N. & Vanderbilt, D. Maximally localized generalized Wannier functions for composite energy bands. *Phys. Rev. B* **56**, 12847–12865 (1997).
22. Souza, I., Marzari, N. & Vanderbilt, D. Maximally localized Wannier functions for entangled energy bands. *Phys. Rev. B* **65**, 1–13 (2002).
23. Pizzi, G. et al. Wannier90 as a community code: New features and applications. *J. Phys.: Condens. Matter* **32**, 165902 (2020).
24. Wahl, R., Vogtenhuber, D. & Kresse, G. $SrTiO_3$ and $BaTiO_3$ revisited using the projector augmented wave method: Performance of hybrid and semilocal functionals. *Phys. Rev. B* **78**, 104116 (2008).

25. Skelton, J. M. et al. Influence of the exchange-correlation functional on the quasi-harmonic lattice dynamics of II-VI semiconductors. *J. Chem. Phys.* **143**, 064710 (2015).
26. Hua, X., Hao, S. & Wolverton, C. First-principles study of vibrational entropy effects on the PbTe-SrTe phase diagram. *Phys. Rev. Mater.* **2**, 095402 (2018).
27. Chaput, L. Direct solution to the linearized phonon boltzmann equation. *Phys. Rev. Lett.* **110**, 265506 (2013).
28. Whalley, L. D., Skelton, J. M., Frost, J. M. & Walsh, A. Phonon anharmonicity, lifetimes, and thermal transport in $CH_3NH_3PbI_3$ from many-body perturbation theory. *Phys. Rev. B* **94**, 220301 (2016).
29. Skelton, J. M. et al. Lattice dynamics of the tin sulphides $SnS_2$, SnS and $Sn_2S_3$: Vibrational spectra and thermal transport. *Phys. Chem. Chem. Phys.* **19**, 12452–12465 (2017).
30. Haque, E. & Hossain, M. A. Origin of ultra-low lattice thermal conductivity in $Cs_2BiAgX_6$ (X = Cl, Br) and its impact on thermoelectric performance. *J. Alloy. Compd.* **748**, 63–72 (2018).
31. Agne, M. T., Hanus, R. & Snyder, G. J. Minimum thermal conductivity in the context of diffuson-mediated thermal transport. *Energy Environ. Sci.* **11**, 609–616 (2018).
32. Liu, T. et al. Unusual thermal boundary resistance in halide perovskites: a way to tune ultralow thermal conductivity for thermoelectrics. *ACS Appl. Mater. Interfaces* **11**, 47507–47515 (2019).
33. Lee, W. et al. Ultralow thermal conductivity in all-inorganic halide perovskites. *Proc. Natl. Acad. Sci.* **114**, 8693–8697 (2017).
34. Mukhopadhyay, S. et al. Two-channel model for ultralow thermal conductivity of crystalline $Tl_3VSe_4$. *Science* **360**, 1455–1458 (2018).
35. Xia, Y., Pal, K., He, J., Ozoliņš, V. & Wolverton, C. Particlelike phonon propagation dominates ultralow lattice thermal conductivity in crystalline $Tl_3VSe_4$. *Phys. Rev. Lett.* **124**, 065901 (2020).
36. Hellman, O., Abrikosov, I. & Simak, S. Lattice dynamics of anharmonic solids from first principles. *Phys. Rev. B* **84**, 180301 (2011).
37. Tadano, T. & Tsuneyuki, S. Self-consistent phonon calculations of lattice dynamical properties in cubic $SrTiO_3$ with first-principles anharmonic force constants. *Phys. Rev. B* **92**, 054301 (2015).
38. Ruske, F. et al. Improved electrical transport in Al-doped zinc oxide by thermal treatment. *J. Appl. Phys.* **107**, 013708 (2010).
39. Kim, C. E. et al. Effect of carrier concentration on optical bandgap shift in ZnO: Ga thin films. *Thin Solid Films* **518**, 6304–6307 (2010).
40. Aydin, E. et al. Zr-doped indium oxide (IZRO) transparent electrodes for perovskite-based tandem solar cells. *Adv. Funct. Mater.* **29**, 1901741 (2019).
41. Liu, Y. et al. Solution processed W-doped $In_2O_3$ thin films with high carrier mobility. *Ceram. Int.* **46**, 2173–2177 (2020).
42. Ellmer, K. Past achievements and future challenges in the development of optically transparent electrodes. *Nat. Photon.* **6**, 809–817 (2012).
43. Frost, J. M. Calculating polaron mobility in halide perovskites. *Phys. Rev. B* **96**, 195202 (2017).
44. Ganose, A. M. et al. Efficient calculation of carrier scattering rates from first principles. Preprint at http://arxiv.org/abs/2008.09734 (2020).
45. Chung, D.-Y. et al. $CsBi_4Te_6$: A high-performance thermoelectric material for low-temperature applications. *Science* **287**, 1024–1027 (2000).
46. Lin, J. et al. Unexpected high-temperature stability of $\beta$-$Zn_4Sb_3$ opens the door to enhanced thermoelectric performance. *J. Am. Chem. Soc.* **136**, 1497–1504 (2014).
47. Zhao, L.-D. et al. Ultralow thermal conductivity and high thermoelectric figure of merit in SnSe crystals. *Nature* **508**, 373–377 (2014).
48. Jong, U.-G., Yu, C.-J., Ri, J.-S., Kim, N.-H. & Ri, G.-C. Influence of halide composition on the structural, electronic, and optical properties of mixed $CH_3NH_3Pb(I_{1-x}Br_x)_3$ perovskites calculated using the virtual crystal approximation method. *Phys. Rev. B* **94**, 125139 (2016).
49. Jung, Y.-K., Lee, J.-H., Walsh, A. & Soon, A. Influence of Rb/Cs cation-exchange on inorganic Sn halide perovskites: from chemical structure to physical properties. *Chem. Mater.* **29**, 3181–3188 (2017).
50. Benin, B. M. et al. Highly emissive self-trapped excitons in fully inorganic zero-dimensional tin halides. *Angew. Chem. Int. Ed.* **130**, 11499–11503 (2018).
51. Daniels, L. M. et al. Phonon-glass electron-crystal behaviour by A site disorder in n-type thermoelectric oxides. *Energy Environ. Sci.* **10**, 1917–1922 (2017).
52. Gurunathan, R., Hanus, R. & Snyder, G. J. Alloy scattering of phonons. *Mater. Horiz.* **7**, 1452–1456 (2020).
53. Xie, H. et al. All-inorganic halide perovskites as potential thermoelectric materials: dynamic cation off-centering induces ultralow thermal conductivity. *J. Am. Chem. Soc.* **142**, 9553–9563 (2020).
54. Togo, A. & Tanaka, I. First principles phonon calculations in materials science. *Scr. Mater.* **108**, 1–5 (2015).
55. Togo, A., Chaput, L. & Tanaka, I. Distributions of phonon lifetimes in Brillouin zones. *Phys. Rev. B* **91**, 094306 (2015).
56. Skelton, J. M. Phono3py-Power-Tools. https://github.com/skelton-group/Phono3py-Power-Tools (accessed 9 February 2021).
57. Madsen, G. K. H., Carrete, J. & Verstraete, M. J. BoltzTraP2, a program for interpolating band structures and calculating semi-classical transport coefficients. *Comput. Phys. Commun.* **231**, 140–145 (2018).
58. Kohn, W. & Sham, L. J. Self-consistent equations including exchange and correlation effects. *Phys. Rev.* **140**, A1133–A1138 (1965).
59. Kresse, G. & Furthmüller, J. Efficient iterative schemes for abinitio total-energy calculations using a plane-wave basis set. *Phys. Rev. B* **54**, 11169–11186 (1996).
60. Kresse, G. & Furthmüller, J. Efficiency of ab-initio total energy calculations for metals and semiconductors using a plane-wave Basis Set. *Comput. Mater. Sci.* **6**, 15–50 (1996).
61. Kresse, G. & Joubert, D. From ultrasoft pseudopotentials to the projector augmented-wave method. *Phys. Rev. B* **59**, 1758–1775 (1999).
62. Blöchl, P. E. Projector augmented-wave method. *Phys. Rev. B* **50**, 17953–17979 (1994).
63. Perdew, J. P. et al. Restoring the density-gradient expansion for exchange in solids and surfaces. *Phys. Rev. Lett.* **100**, 136406 (2008).
64. Heyd, J., Scuseria, G. E. & Ernzerhof, M. Hybrid functionals based on a screened coulomb potential. *J. Chem. Phys.* **118**, 8207–8215 (2003).
65. Krukau, A. V., Vydrov, O. A., Izmaylov, A. F. & Scuseria, G. E. Influence of the exchange screening parameter on the performance of screened hybrid functionals. *J. Chem. Phys.* **125**, 224106 (2006).

## ACKNOWLEDGEMENTS

We thank J.M. Skelton and A.M. Ganose for useful discussions on phonon and electron transport. Via our membership of the UK's HEC Materials Chemistry Consortium, which is funded by EPSRC (EP/L000202), this work used the ARCHER UK National Supercomputing Service (http://www.archer.ac.uk). This work was supported by a National Research Foundation of Korea (NRF) grant funded by the Korean government (MSIT) (No. 2018R1C1B6008728). This research was partially supported by the Graduate School of YONSEI University Research Scholarship Grants in 2019.

## AUTHOR CONTRIBUTIONS

Y.-K.J. performed the calculations, collected, and analyzed the data. I.T.H. and Y.C.K. initialized the project. A.W. led the project. All authors contributed to discussing the results and writing the manuscript.

## COMPETING INTERESTS

The authors declare no competing interests.

## ADDITIONAL INFORMATION

**Supplementary information** The online version contains supplementary material available at https://doi.org/10.1038/s41524-021-00521-9.

**Correspondence** and requests for materials should be addressed to Y.C.K. or A.W.

**Reprints and permission information** is available at http://www.nature.com/reprints

**Publisher's note** Springer Nature remains neutral with regard to jurisdictional claims in published maps and institutional affiliations.